

PAPER • OPEN ACCESS

Nanodiamond surface as a photoluminescent pH sensor

To cite this article: Yaraslau Padrez *et al* 2023 *Nanotechnology* **34** 195702

View the [article online](#) for updates and enhancements.

You may also like

- [Combinatorial approaches to evaluate nanodiamond uptake and induced cellular fate](#)
Reem Eldawud, Manuela Reitzig, Jörg Opitz *et al.*
- [Plasmon-modulated photoluminescence enhancement in hybrid plasmonic nano-antennas](#)
Alireza R Rashed, Mohsin Habib, Nekhel Das *et al.*
- [In vitro characterization of osteoblast cells on polyelectrolyte multilayers containing detonation nanodiamonds](#)
Sascha Balakin, Young-Shik Yun, Jihye Lee *et al.*

PRIME
PACIFIC RIM MEETING
ON ELECTROCHEMICAL
AND SOLID STATE SCIENCE










HONOLULU, HI
Oct 6–11, 2024

Abstract submission deadline:
April 12, 2024

Learn more and submit!

Joint Meeting of
The Electrochemical Society
•
The Electrochemical Society of Japan
•
Korea Electrochemical Society

Nanodiamond surface as a photoluminescent pH sensor

Yaraslau Padrez^{1,*} , Lena Golubewa^{1,2} , Anastasiya Bahdanava¹ , Marija Jankunec³ , Ieva Matulaitiene⁴ , Dmitry Semenov⁵, Renata Karpicz¹ , Tatsiana Kulahava¹ , Yuri Svirko²  and Polina Kuzhir² 

¹ Department of Molecular Compounds Physics, State research institute Center for Physical Sciences and Technology, Vilnius, Lithuania

² Department of Physics and Mathematics, Center for Photonics Sciences, University of Eastern Finland, Joensuu, Finland

³ Institute of Biochemistry, Life Sciences Center, Vilnius University, Vilnius, Lithuania

⁴ Department of Organic Chemistry, State research institute Center for Physical Sciences and Technology, Vilnius, Lithuania

⁵ School of Computing, Faculty of Science and Forestry, University of Eastern Finland, Kuopio, Finland

E-mail: yaraslau.padrez@ftmc.lt and polina.kuzhir@uef.fi

Received 17 November 2022, revised 29 January 2023

Accepted for publication 6 February 2023

Published 3 March 2023



CrossMark

Abstract

A systematic spectroscopic characterization of highly homogeneous water suspensions of ‘buckydiamonds’ comprising sp^3 cubic nanodiamond (ND) core covered with disordered sp^2 shell densely decorated with oxygen-containing groups demonstrates the excitation-wavelength-dependent photoluminescence (PL) given by at least four types of specific structures on the ND surface (hydroxyl, C=O containing ketones, carboxylic anhydrides, and carboxyl groups). PL properties of NDs suspensions possess concentration-dependent behavior revealing tendency of NDs to agglomerate. PL of NDs has been found to be strongly sensitive to pH of the environment in wide range of pH values, i.e. 2–11. We disclosed the mechanisms of pH sensitivity of the ‘buckydiamond’ and proved that it can serve as all-optical sensor of tiny pH variations suitable for further exploitation for pH sensing locally in the area where NDs have been delivered for any purpose, e.g. bioimaging or therapeutic needs.

Supplementary material for this article is available [online](#)

Keywords: nanodiamonds, photoluminescence, oxygen-containing groups, surface chemistry, pH sensing

(Some figures may appear in colour only in the online journal)

1. Introduction

Nanodiamonds (NDs) have a promising sensing potential. It may rely on point-like defects of the diamond lattice due to implanted ‘guest’ atoms (e.g. N, Si, etc) [1], or intrinsic

defects (e.g. lattice vacancies) [2, 3] originating from ND synthesis [4, 5] and/or post-synthesis treatment [6–8]. These defects form so-called color centers, which possess a strong temperature-dependent (SiV [9], GeV [10] color centers) and spin-dependent (NV color centers) photoluminescence (PL) [11], show no blinking [12] or photobleaching [13], demonstrate sensitivity to free radical formation in living cells [14–16] and chemical reactions at ambient conditions [17] or changes in pH environment [18]. In combination with NDs chemical inertness inherited from bulk diamond, all mentioned functionalities make NDs attractive for bio-medical applications. However in order to penetrate the cell membrane

* Author to whom any correspondence should be addressed.



Original content from this work may be used under the terms of the [Creative Commons Attribution 4.0 licence](#). Any further distribution of this work must maintain attribution to the author(s) and the title of the work, journal citation and DOI.

[19], and to be employed in high resolution microscopy at a single molecule level [20] the ND size should be less than 10 nm.

Size, quality and functional properties of NDs strongly depend on the method of their synthesis. At present, most of commercial NDs are fabricated at (i) high pressure and high temperature (HPHT) conditions, (ii) via detonation, or (iii) pulsed laser ablation (PLA) processes [21].

The HPHT, which is based on the grinding of micron-sized HPHT diamonds, gives high-quality NDs having of >10 nm size [22]. Both other methods allow obtaining considerably smaller particles, however, the detonation nanodiamonds (DNDs) synthesis can be hardly controlled, has a low yield [23, 24], and requires purification of DNDs from metallic impurities [25], their de-agglomeration and fractionation [26, 27]. In contrast, the PLA is environmentally friendly, non-hazardous [28] and enables the control of the size, morphology, and shape of the NDs, which are metal-free [29]. The latter is especially essential for biomedical applications because metal impurities make chemically inert NDs deadly toxic because Fe impurities induce the production of highly cytotoxic hydroxyl radicals ($\text{HO}\cdot$) in the Fenton reaction of H_2O_2 with Fe^{2+} [30] leading to oxidative stress and damage of biomolecules involved in redox cycling in cells [31]. Moreover, both HPHT NDs and DNDs exhibit mainly hydrophobic properties and collapse into lumps in polar solvents, such as water or saline. Post-synthesis functionalization is needed to overcome the agglomeration processes.

In PLA NDs, the formation of sp^2 shell around the sp^3 core occurs as the temperature and pressure inside the ablation plume decrease below those required for the sp^3 phase formation [32]. PLA synthesis of NDs in the liquid phase supports the appearance of additional functional groups on the ND surface, simplifying the ND solvation and stabilizing the suspension. Moreover, the presence of surface functional groups is essential for further surface modification, functionalization, or conjugation needed for specific biomedical tasks [33]. At the same time, variety of oxygen-containing groups on the ND surface may substantially complicate the interpretation of spectroscopic data.

In this paper we demonstrate how the diverse assortment of functional groups on the ND surface can be employed for all-optical pH sensing by exploring sensitivity of the oxygen-containing surface groups photoluminescence to the pH variations. In contrast to the existing complex approaches based on the spin relaxation of NV^- color centers in conjugates of NDs with pH-cleavable linkers [34], the proposed technique is much simpler and can be easily transferred to biomedicine and employed both at a single-cell level *in vitro* or at an organism level *in vivo*.

2. Materials and methods

NDs (RayND-M-W2) produced by Light Hydro-Dynamic Pulse (LHDP) technology [35], a PLA technique that employs hydrocarbon composite and light pulses at 1064 nm wavelength from the Nd:YAG laser, were kindly provided by Ray

Techniques Ltd (Israel). To form stable NDs suspension in water the stabilizing surfactant TDW (Ray Techniques Ltd, Israel) was used by the manufacturer. According to product description, the average ND size is 4–4.5 nm.

Transmission electron microscopy (TEM) was performed using a TitanG2 60–300 electron microscope (FEI Co., The Netherlands).

Atomic Force Microscopy (AFM) imaging was carried out in a tapping mode on a Dimension Icon scanning probe microscope system (Bruker, Santa Barbara, CA, USA) at room temperature (20 ± 0.5 °C) using silicon AFM probes FESPA-V2 (Bruker, Santa Barbara, CA, USA).

Fourier transform infrared (FTIR) spectra were recorded using an ALPHA spectrometer (Bruker, INC., Bremen, Germany), equipped with a DLATGS detector, operated at room temperature. The samples were measured in attenuated total reflectance (ATR) mode. Spectra were averaged from 100 scans; spectral resolution was set at 4 cm^{-1} in the range from 400 to 4000 cm^{-1} , with air used as a reference. $10 \mu\text{l}$ of NDs suspension or $40 \mu\text{l}$ of TDW were dropped onto a diamond crystal. Measurements were performed from dry residue after full evaporation of water.

Raman spectra of NDs were obtained using the Raman Flex spectrometer (Perkin Elmer, UK). Measurements were performed for ND water suspension (wt 2%), NDs on a polished Si wafer dried in the air atmosphere at room temperature or after annealing at 450 °C in the air atmosphere for 8 h. Spectra were collected from at least three different points on each sample and then averaged. Raman signal accumulation time was 10 s per 10 cycles. A 785 nm diode laser of $9.0 \mu\text{W}$ power was used as an excitation source.

Surface enhanced Raman spectroscopy (SERS) of the ND suspensions was done using black silicon (bSi) covered with gold as a SERS-active substrate. bSi represents a highly developed rough surface with micron-sized silicon cones, which, being coated with gold (bSi-Au), serve as ‘hot-spots’ for SERS, making the bSi-Au substrate SERS-active [36]. Recently, bSi-Au was successfully applied for characterization of graphene quantum dots (GQDs) [37].

Ultraviolet–visible (UV–vis) absorbance spectra of ND water suspensions were measured in a 1 cm pathlength quartz cuvette using UV–vis spectrophotometer JASCO V-670 (Jasco, USA).

The PL spectra and PL characteristic lifetimes were measured using time-correlated single-photon-counting fluorescence spectrometer F900 (Edinburgh Instruments Ltd, UK). Semiconductor diode lasers EPL-470 (Edinburgh Instruments, Ltd, UK) with pulse duration 71.7 ps, wavelength 472.8 nm, repetition rate of 5 MHz, pulse energy $49 \mu\text{W}$ and EPL-375 (Edinburgh Instruments, Ltd, UK) with pulse duration 57.3 ps, wavelength 371.0 nm, repetition rate of 5 MHz, pulse energy $140 \mu\text{W}$ were used as excitation sources. The signal accumulation time was 2 s.

Measurements were performed at room temperature in 1 cm quartz cuvettes. In order to obtain the characteristic lifetimes of the PL, time decay curves were fitted using Edinburgh advanced lifetime analysis software with the

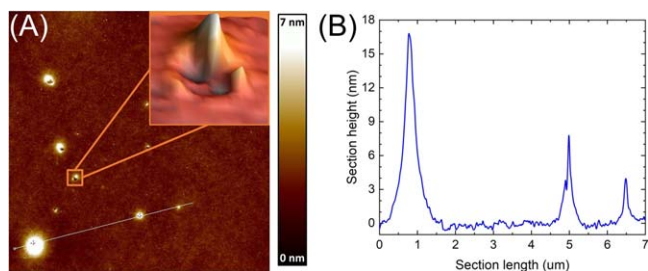


Figure 1. AFM images of NDs spin-coated on the polished Si wafer: (A)—height distribution, (B)—height sectioning along the white line in (A). The Scan area is $10 \times 10 \mu\text{m}$. Inset in (A) gives a 3D reconstruction of the ND with an artifact ‘ring’ around the particle caused by a polymer matrix around the particle.

following function (1):

$$Fit = A + B_1 \cdot e^{-\frac{t}{\tau_1}} + B_2 \cdot e^{-\frac{t}{\tau_2}}, \quad (1)$$

where characteristic lifetimes τ_1 and τ_2 are the PL decay fast and slow components, A and $B_{1,2}$ are background signal and pre-exponential factors, respectively.

The measurement of the dependence of PL spectra on the excitation wavelength (photoluminescence excitation (PLE) mapping) for two ND concentrations (0.01% and 0.04%) and the same TDW concentrations have been carried out on a Fluorescence Spectrometer FL8500 (Perkin Elmer Inc., USA). The continuous xenon arc lamp was used as an excitation source. Excitation wavelengths were varied from 210 to 546 nm with 4 nm step. Emission wavelengths were ranged from 320 to 720 nm with 0.1 nm step. The excitation and emission slit widths were 5 nm. Scan speed was 240 nm per minute. A long pass emission filter 320 nm was used. Photomultiplier voltage was adjusted to 550 V.

Direct measurements of the pH phosphate buffer solutions (PBS) were performed using pH-meter FiveEasy FE20 with Electrode LE438 (Mettler Toledo, Switzerland). The pH values of PBS varied from 2.14 to 10.56 by addition of HCl or NaOH.

3. Result and discussion

3.1. Structural characterization of NDs

Structural characterization of the ND suspensions was performed by means of TEM, AFM, ATR-FTIR and Raman (SERS) spectroscopies.

The TEM micrographs of NDs are presented in figure S1 (supplementary material). Although the detection of the diamond structure was significantly complicated by a huge graphitic-polymer coat (the origin and content of the coat will be enclosed and discussed in further section), $\{111\}$ planes of the diamond structure ($d_{111} \approx 0.210 \text{ nm}$) are recognizable and confirmed by the gray-level profiling (see figure S1(B), supplementary material).

AFM measurements allowed revealing the characteristic dimensions of the NDs in suspensions (see figure 1). The average height of single NDs equals to 6.61 nm, however

some agglomerates of height around 15 nm are present. The appearance of some artefact ‘ring’ around the single particle (see the inset in figure 1(A)) and excess of the diameter of the registered particles over their height are due to stabilizing surfactant TDW (for statistical data and more details see in supplementary material, section 2).

In order to characterize the ND shell and functional groups, which were formed on the ND surface after stabilizing the suspension, the FTIR spectra were recorded (figure S2). In the high frequency region, we observe bands at 3246 cm^{-1} and 3081 cm^{-1} , which are assigned to $\nu(\text{O-H})$ and $\nu(\text{N-H})$ vibrations, respectively [38], and bands around 2946 and 2884 cm^{-1} belonging to symmetric and asymmetric $\nu(\text{CH}_2)$ vibrations, respectively. The latter bands are often associated with the edges in graphitic material. The most intense band centered at 1658 cm^{-1} originates from the overlapping of $\nu(\text{C=C})$ vibration in the sp^2 graphitic materials and $\delta(\text{O-H})$ [39, 40].

The other band that belongs to graphene-like materials is located near 1430 cm^{-1} and assigned to $\delta(\text{C-H}) \text{ sp}^2$ hybridized carbon [39, 41]. Low intensity band at 1772 cm^{-1} belongs to non-conjugated ketone [41]. The bands at 1380 and 1280 cm^{-1} are assigned to $\nu(\text{C-O-C})$ in carboxylic anhydrides, the band at 1116 cm^{-1} and a shoulder at 1260 cm^{-1} indicate the presence of epoxy groups [39, 42].

In addition, FTIR spectrum of solvent TDW, used for stabilizing ND water suspension, was registered. After water evaporation, the thin film of dried solvent was formed on the ATR crystal. The broad band centered at 3326 cm^{-1} is assigned to $\nu(\text{O-H})$, $\nu(\text{N-H})$ and $\nu(\text{C-H})$ vibrations, associated with polymeric material [43]. Non-intensive bands at $2800\text{--}3000 \text{ cm}^{-1}$ belong to $\nu(\text{CH}_2)$ and $\nu(\text{CH}_3)$ vibrations and are typical to hydrocarbon chain. As these bands are non-intensive, the hydrocarbon chains are non-dominant in the material. The band around 2340 cm^{-1} belongs to CO_2 adsorbed from the atmosphere [43]. The band at 1648 cm^{-1} was assigned to $\nu(\text{C=O})$ in amide I, and $\delta(\text{O-H})$ of not evaporated water [40, 44, 45]. The most intensive bands near 1415 cm^{-1} with the shoulder at 1450 cm^{-1} were assigned to $\delta(\text{C-H})$ and $\nu(\text{C-N})$ vibrations, respectively [46]. The epoxy groups are also present in the solvent spectrum at 1116 cm^{-1} . The sharp band at 873 cm^{-1} is assigned to $\nu(\text{C-H})$ [43].

The sp^3 and sp^2 carbon allotropes in the samples were analyzed using Raman spectroscopy. The low concentration of NDs (wt 2%) in the suspension, presence of TDW and strong fluorescent signal from the oxygen-containing groups decorating the ND surface complicates analysis of the Raman spectrum of the suspension (see figure 2(A), spectrum 1).

In order to reveal Raman signal associated with carbon materials, TDW residues were removed by annealing of the NDs layer on Si wafer at $450 \text{ }^\circ\text{C}$ for 8 h in air atmosphere. Such annealing does not affect the ND itself because diamond degradation occurs at temperatures higher than $500 \text{ }^\circ\text{C}$ [47]. Annealing in the presence of oxygen may cause some etching of sp^2 phases as well as surface functional groups, leading to the disappearance of a strong fluorescent background. However, there are two characteristic peaks in the Raman spectrum of annealed NDs (see figure 2(A), spectrum 2). They are

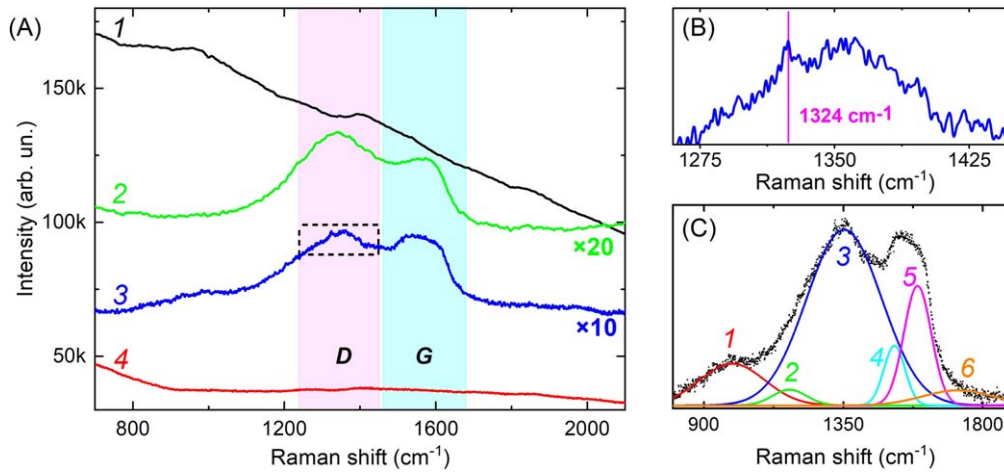


Figure 2. (A) Raman spectra of NDs water suspension (1), annealed NDs layer on Si wafer (2), annealed NDs on bSi-Au (3), and non-annealed NDs layer on Si wafer (4). (B) Dashed rectangle in figure (A); (C) Gauss approximation of 800–1900 cm^{-1} , with maxima positions centered at: 1–992 cm^{-1} (2nd order Raman band of Si, from the bSi-Au substrate), 2–1176 cm^{-1} (C–O, from defects on sp^2 -disordered shells [56]), 3–1352 cm^{-1} (disordered or amorphous phases, D-band), 4–1515 cm^{-1} (iTO phonon near $1/4 \Gamma\text{K}$, appears in SERS spectrum [56]) 5–1590 cm^{-1} (G-band of graphitic carbon), 6–1720 cm^{-1} (C=O). All spectra were obtained in the same conditions. A 785 nm laser diode was used as an excitation source.

assigned to (i) disordered or amorphous phases (D band, centered at 1352 cm^{-1}) and (ii) defective sp^2 graphite-like structures (the E_{2g} symmetry allowed G-band, centered at 1590 cm^{-1}). The absence of the first-order diamond band normally located at 1330 cm^{-1} is more likely explained by small size of the NDs, namely high relative fraction of sp^2 phase comparing to sp^3 one [48]. Nevertheless, the impact of the first-order diamond band in the total spectrum may be negligible, as the Raman scattering cross section of sp^2 -disordered shells is much higher than that of sp^3 cubic lattice [49].

The SERS spectrum of the annealed NDs is shown in figure 2(A), spectrum 3. In contrast to the Raman spectrum of annealed NDs (figure 2(A), spectrum 2), in the SERS spectrum, the first-order diamond Raman band is present being shifted from 1330 to 1324 cm^{-1} (figure 2(B)) as was previously observed for SERS spectra of NDs [50] and thin ultradispersed diamond layers [51]. Such a ‘red’ shift of the diamond Raman band is due to the phonon confinement effect [52]. It is worth noting that application of bSi-Au SERS-substrate allowed to reveal the presence of C=O groups centered at 1720 cm^{-1} (see figure 2(C)) [53]. The spectra of NDs obtained by laser ablation process are consistent with the experimental results for detonation NDs [54], indicating their similarity to onion-like shells with diamond cores known as ‘buckydiamonds’ [55] (the model is presented in figure S3).

The average distance between the defects, which represents the size of the sp^2 domains, was calculated according to the formula [57]:

$$L_D = \sqrt{5.4 * 10^{-2} * E_\lambda \left(\frac{I_D}{I_G} \right)}, \quad (2)$$

where E_λ is the excitation laser energy in eV, I_D is the D-band intensity, and I_G is the G-band intensity. According to the performed estimations, $L_D = 0.62$ nm. It indicates the small size of carbon flakes and a large number of defects associated

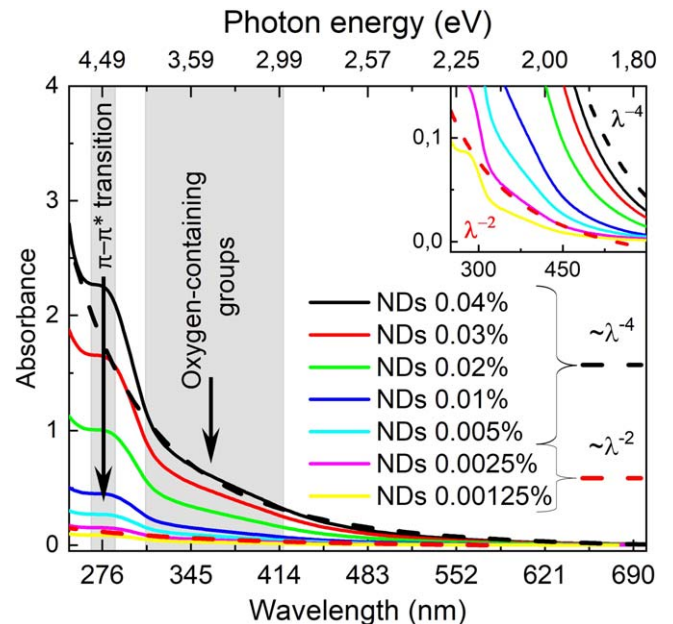


Figure 3. The absorption spectra of water suspensions of different concentrations of NDs. Inset—enlarged area which corresponds to low concentrations of NDs.

with oxygen groups. Proposed structure of disordered sp^2 -domains of graphene-like shells on sp^3 -phase are presented in figure S3 (supplementary material).

The results of full characterization of NDs structure are collected in table S2 (supplementary material), related discussion see in supplementary materials.

3.2. Spectroscopic characterization of NDs

The UV–vis absorption spectra of suspensions having NDs concentrations from 0.00125% to 0.04% show two prominent maxima (see figure 3). The first absorption peak, which is

centered at 276 nm (4.5 eV), is lower than the bandgap of the impurity-free crystalline diamond at 5.5 eV [58]. It is related to the π - π^* transition in sp^2 -hybridized carbon atoms in clusters surrounding sp^3 -phase [59]. The second broad, but less pronounced band centered at 390 nm (approx. 3.0–4.0 eV) is associated with the presence of oxygen-containing functional groups (C=O/COOH/C–O–C) on the graphitic shell covering ND surface [60]. Intermediate non-bonding (n) states in oxygen-containing groups arise within the π - π^* energy gap and are responsible for the n - π^* electronic transition in absorbance spectra [61].

At high (0.005%–0.04%) NDs concentrations, the wavelength dependence of the absorbance of the suspension is well described by λ^{-4} law indicating that Rayleigh scattering dominates [62–64]. At lower concentrations, the absorption of light by the sp^2 conducting layer on the surface of NDs prevails leading to the λ^{-2} absorbance at longer wavelength [65].

To reveal the origin of NDs PL, we studied the PL spectra in wide ranges of the excitation (210–546 nm, 4 nm step) and emission (320–720 nm) wavelengths. The obtained results are presented as 2D PLE false color maps in figure 4. One can observe from figure 4(A) (2D PLE map and the right panel with PLE spectra) that there are three pronounced (4.96 eV, 3.80 eV and 3.46 eV) and two weak (2.97 eV and 2.68 eV) absorption peaks. The latter peaks become observable at the high concentrations of NDs (0.04% wt) (figure 4(B)).

Comparison of the shape and position of the first PLE peak (4.96 eV) and the first maximum in UV–vis absorbance spectra (4.50 eV, see figure 3) reveals that in the range 250–290 nm, Rayleigh scattering dominates. The interband transition at 4.96 eV is not resolved in the UV–vis absorbance spectrum since scattering cross-section in the UV range significantly exceeds the absorption one of the sp phase. In the PLE spectra the peak at 4.96 eV can be observed because the PL photon energy is lower than excitation one, i.e. the Rayleigh background can be filtered out.

Electronic transitions with energies around 4.96 eV led to further radiative transitions in wide spectral range (320–670 nm) with comparable efficiencies for both analyzed NDs concentrations (figures 4(A) and (B)), with a red shift of the absorptive transition to 4.80 eV at increase of the NDs content. These optical transitions more likely occur from the bottom of the valence band to the conduction band in so-called Pandey chains (conjugated alkadienes). These chains are dimer chains on the facets of a diamond core [60] and edges of the sp^2 -carbon clusters in the shell shown in figure S4 (Supplementary Material). Due to high defectiveness of the shell and the resemblance of this sp^2 -clusters to graphene oxide quantum dots (GOQDs), transition at 4.96 eV, which is higher in energy than π - π^* transition (4.50 eV) observed in UV–vis absorbance spectra, may also arise from n - σ^* transition in sp^3 -domains associated with hydroxyls or ethers, as reported in [61]. At higher concentrations of NDs the PL intensity with excitation at energies around 4.96 eV preserves its magnitude indicating that this PL originates from the sp^3 diamond core of NDs. It is so because some of the NDs (and their sp^3 core) appear to be screened from the excitation light

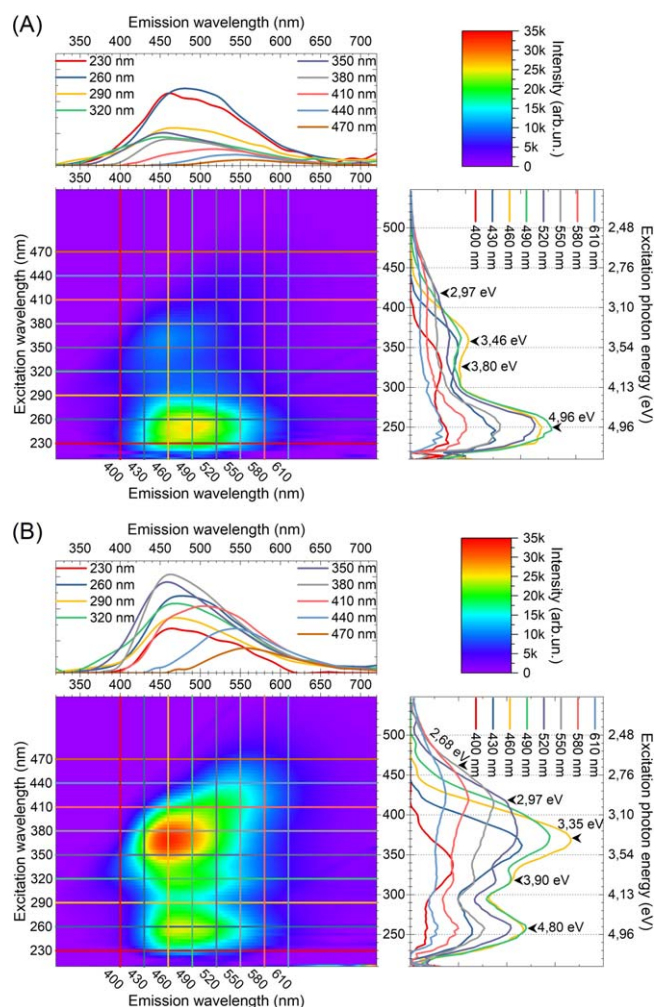


Figure 4. PLE-maps and image profiles of (A) 0.01% and (B) 0.04% ND water suspensions. Upper panels correspond to PL spectra taken at excitation in the range 230–470 nm with 30 nm step; right panels correspond to PLE spectra measured at emissions from 400 to 610 nm with 30 nm shift. Maxima in PLE spectra are marked with ticks, positions are represented in eV.

due to agglomeration of the core–shell NDs particles and light does not reach the inner NDs and their sp^3 cores. Very similar behavior was observed, e.g. for semiconducting quantum dots in [66].

Other bands in PLE mapping are in good correspondence with the observed broad band in the absorbance spectrum (see figure 3) around 390 nm. They originate from sp^2 -clusters on the ND shell decorated with edge oxygen-containing groups and are in agreement with the results for GOQDs reported in [61]. The long wavelength peaks at 3.80 eV, 3.46 eV and 2.97 eV are more likely arising from n - π^* transition in oxygen-containing groups in sp^2 clusters of the ND shell.

PLE strongly depends on the NDs concentration. It manifests itself in significant increase in the PL intensity under excitation in the range of 300–500 nm. Maxima in PLE spectra undergo a blue shift from 3.80 eV to 3.90 eV and a red shift from 3.46 to 3.35 eV. The peak at 2.97 eV is not shifted, but PL intensity also increases, and new peak at 2.68 eV appears. Blue or red shifts in the PL spectra indicate that

some physical properties of the system have changed, leading to the change in the interband transitions. When the ND concentration increases, this change may indicate either the formation of ND agglomerates or manifestation of the so-called inner filter effect. The latter occurs in highly concentrated solutions when the excitation beam is attenuated by the sample so that only the sample surface layer facing the incident beam fluoresces. This phenomenon has been observed in e.g. aqueous dispersion of semiconductor quantum dots [67]. We suggest that in the UV excitation, the blueshift (hypsochromic shift) is due to NDs agglomeration, which shields sp^3 phase from the polar solvent (water). It reduces the effect of dipolar relaxation in the inner part of the ND agglomerate [68]. Contrary, in the NIR-versus wavelength region, the redshift (or bathochromic shift) at high ND concentrations is due to the inner filter effect [67], i.e. efficient fluorescence only by the surface facing the radiation because the excitation light is unable to penetrate the bulk of the sample. It is worth noting that dipolar relaxation may also contribute to the observed concentration dependence of the spectra as sp^2 carbon nanosheets passivated with oxygen-containing groups act as dipoles interacting on the outer layer of the core-shell NDs agglomerates. In particular, sp^2 -shells on the top of NDs is very similar to those of the Prodan dye, which shows significant PL redshift when dispersed in more polar solvent [68].

The PL peak around 2.68 eV may have excitonic nature and originate from the graphene-like islands strongly passivated with oxygen-containing groups. This hypothesis is supported by the PLE mapping of GQDs accompanied by density functional theory simulations in [69]. It has been demonstrated that excitation-dependent PL in NIR arises from various sizes of sp^2 carbon cluster states, and excitonic properties are caused by the quantum confinement. Moreover, these states are strongly dependent on the surrounding media such as H^+ concentration around the oxygen-containing functional groups. Increase of the intensity of long wavelength PL at higher concentrations of NDs (compare figures 4(A) and (B)) has more likely the same nature and is induced by the interaction between neighboring particles causing changes in sp^2 carbon cluster excitonic states.

To sum up, PLE maxima at 4.96 eV arises from sp^3 core, while other transitions are consequences of the presence of highly defective shell. PLE mapping of TDW solution demonstrates no influence on the spectroscopic characteristics of NDs suspensions (see figure S4, supplementary material).

One can observe from figures 4(A) and (B) (upper panels) that NDs suspensions exhibit excitation-wavelength-dependent PL. PL spectra fitting with multiple Gaussian profiles reveals the presence of several independent PL centers in NDs, which we will name further as ‘UV’, ‘Blue’, ‘Green’ and ‘Orange’ bands according to the maximum position (supplementary material, figures S5(A) and S5(B)). The maximum positions slightly red-shift with the increase of the excitation wavelength. Dependence of the emission on the excitation wavelength indicates the radiative recombination through the shallow trap states [70, 71], unlike the case of excitation-wavelength-independent PL when irradiative

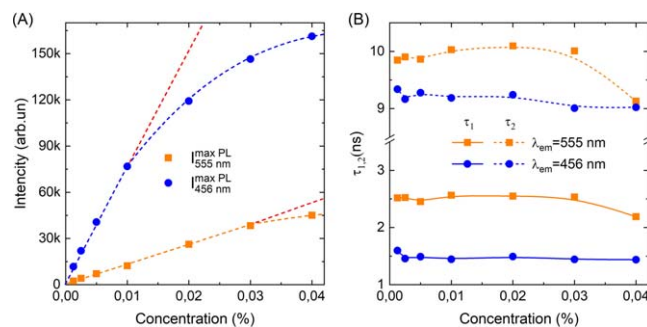


Figure 5. The Dependence of PL characteristics on the NDs concentration in the range from 0.00125% to 0.04%. (A) PL peak intensity, excited at 375 nm (3.31 eV) and 470 nm (2.64 eV) with emission recorded at 555 nm and 456 nm, respectively. (B) The characteristic lifetimes τ_1 and τ_2 of the ND water suspensions, measured in the same conditions.

transition from π^* orbital to n-state occurs after a non-radiative transition of electrons to π^* state [61]. The results of the fitting of PL spectra are presented in figure S5. All identified bands are broad and overlap significantly. For convenience, we name them further ‘UV’, ‘Blue’, ‘Green’ and ‘Orange’ bands. ‘UV’ PL centre is around 380 nm, which is more likely associated with radiative transitions in carbon dimer chains and sp^2 -clusters [72]. ‘Blue’ PL centre maximum position around 450 nm does not change over the whole excitation wavelength range and is more likely assigned to the radiative transitions associated with $-OH$ groups [71].

Dominant impact of the hydroxyl groups in the whole spectrum occurs at excitation wavelengths covering the range 240–420 nm (figure S5, supplementary materials). ‘Green’ and ‘Orange’ bands have a more complex structure and arise from functional groups containing $C=O$, such as ketone, carboxylic anhydride and carboxyl groups, which begin to dominate in the PL spectrum with the increase of the excitation wavelength [71, 73]. This long wavelength region of PL splits in at least two peaks, however, the fitting is significantly complicated, which is likely due to the entangled interactions between the hydroxyl groups (n-state) and carbonyl groups ($\pi^*(CO)$), leading to the red-shift of the peaks with the increase of the excitation wavelength, which is in agreement with the data presented in [70]. However, ‘Orange’ band is associated with $-COOH$ groups [71].

PL intensity of ND suspensions is concentration dependent. Moreover, different PL centers behave differently (see figure 5(A)). Excitation was performed at 375 nm for ‘Blue’ PL centers and at 470 nm for ‘Orange’ PL centers to achieve the best separation of the impact of $-OH$ and $-COOH$ surface groups, respectively. At low concentrations (up to 0.01%), the PL intensity of ‘Blue’ centers increases linearly. At higher ($>0.01\%$) concentrations, the saturation of the PL intensity occurs because the role of scattering and reabsorption increases due to possible agglomeration of NDs at high concentrations. The PL intensity of ‘Green’ centers is a linear function of the NDs concentration in wide range spanning up to 0.03%. This indicates the independence of this PL line from the degree of agglomeration (see figure 5(A)).

Table 1. Origin of the spectroscopic properties of NDs.

ND measurable parameters	Method	Result	References
Optical	UV-vis	Peak positions and transition energies:	
Absorptive	absorptio	–276 nm (4.5 eV)— π - π^* transition in sp^2 -hybridized carbon atoms in	[59]
Transitions	n spectroscopy	clusters surrounding sp^3 -phase [59] –390 nm (approx. 3.0–4.0 eV)— n - π^* electronic transition, associated with C=O/COOH/C–O–C/etc on sp^2 -domains of the ND surface	[60, 61] [65]
		Curve fitting: λ^{-4} (0.04% wt NDs)—Rayleigh scattering contribution λ^{-2} (<0.005% wt NDs)—absorption by surface sp^2 conducting layer	
PL properties	PLE	Effectively emitting absorptive transitions: – 250 nm (4.96 eV, non-observable in UV-vis)—intrinsic states (core): diamond core surface, n - σ^* transition in sp^3 -domains associated with hydroxyls or ethers, Pandey chains	[60, 61] [74] [69]
		– 326 nm (3.80 eV), 358 nm (3.46 eV), 417 nm (2.97 eV)—extrinsic states (shell): n - π^* transition from oxygen-containing groups in sp^2 clusters in the ND shell (C–O–C, OH, carbonyls) –462 nm (2.68 eV)—extrinsic state, excitonic, sp^2 carbon clusters of different sizes, passivated with oxygen-containing groups	
		Concentration dependency: -PL caused by absorptive transitions in extrinsic states increase -PL caused by absorptive transitions in intrinsic states does not change	
	PL	(i) Excitation-wavelength dependent PL (ii) At least four emissive states: UV—380 nm— sp^2 -clusters, intrinsic states Blue—450 nm—radiative transitions associated with –OH groups [71], extrinsic states	[72] [71] [70, 71, 73]
		Green and Orange—around 500 nm and 555 nm, red-shifted with λ_{ex} increase after 400 nm, associated with C=O (ketone, carboxylic anhydride, carboxyl groups), $n(OH)$ - $\pi^*(C=O)$, extrinsic states	
		(iii) Concentration dependent (iv) pH dependent ('Blue' PL (–OH), 'Orange' PL (C=O))	
	PL- τ	Characteristic lifetimes: $\tau_1 = 1.48 \pm 0.06$ ns, $\tau_2 = 9.18 \pm 0.12$ ns ('Blue', –OH, concentration-independent) $\tau_1 = 2.47 \pm 0.13$ ns, $\tau_2 = 9.84 \pm 0.33$ ns, ('Orange', –COOH, concentration-dependent)	

Figure 5(B) shows the dependences of the characteristic lifetimes τ_1 and τ_2 (see equation (1)) of the PL on the ND concentration measured at 456 nm ('Blue') and 555 nm ('Orange') wavelengths with excitation at 375 nm and 470 nm, respectively (see table 1). Both τ_1 and τ_2 for 'Blue' PL centers in NDs, in contrast to 'Blue' PL intensity, are independent of the NDs concentration. The lifetimes for 'Orange' PL centers change only at the ND concentrations above 0.03%, completely repeating the behavior of PL intensities.

Principal spectroscopic characteristics with their origin indication are summarized in table 1.

3.3. Application of ND suspensions for pH sensing

A variety of oxygen-containing functional groups on the surface of NDs provide a solid background for using NDs for sensing of the pH environment. The carboxylic groups –COOH respond to the pH changes via protonation/deprotonation (see figure 6(A)). The C=O and –OH groups participate in hydrogen bonding, resulting in agglomeration/deagglomeration of NDs and NDs' solvation (see figure 6(B)).

To exclude the possible impact of additional agglomeration caused by high concentrations of NDs, suspensions of 0.01% of NDs were used for all further measurements. NDs UV-vis absorption spectra (see figure S6, supplementary materials) as well as short lifetimes measured for 'Blue' PL and 'Orange' PL centers, responsible for –OH and –COOH groups, respectively, are pH-insensitive, while long lifetimes show slight decrease at the pH values below neutral (see figure S7, supplementary materials).

However, PL intensities for both 'Blue' and 'Orange' PL centers demonstrate significant dependence on the pH values in a wide range of pH (see figures 7 (A) and (B)). It is reflected in the decrease of PL intensity at $\lambda_{em} = 456$ nm (excitation at $\lambda_{ex} = 375$ nm) and simultaneous increase of PL intensity at $\lambda_{em} = 555$ nm (excitation at $\lambda_{ex} = 470$ nm).

Intensity increases for 'Orange' PL centers (–COOH groups) occurs at high pH values due to the delocalization of the electron from oxygen in deprotonation, caused by the proton depletion, and the formation of resonance structures in –COO. Different directions of PL intensity changes, when

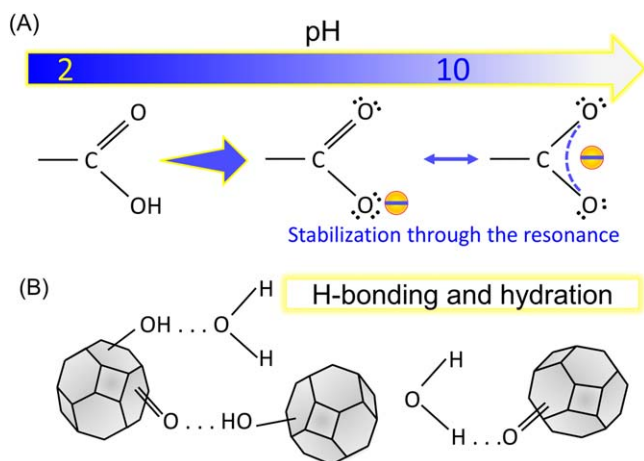


Figure 6. Oxygen-containing groups in water environment: (A) carboxylic group modification at different pH values, (B) H-bonding and hydration.

pH values varies, suggest using the ratio of ‘Blue’ and ‘Orange’ PL intensities for pH measurement to suppress influence of the laser power fluctuations and ND-concentration dependence of the detected signal.

Figure 7(C) shows the obtained calibration curve allowing the determination of the pH values of water ND suspensions by PL measurements. One can observe that the ratio of normalized PL intensities I_{555} measured at $\lambda_{em} = 555$ nm (excitation at $\lambda_{ex} = 470$ nm) and I_{456} $\lambda_{em} = 456$ nm (excitation at $\lambda_{ex} = 375$ nm) is well approximated with a linear function ($R^2 = 0.97$).

The pH value of the solution containing 0.01% of NDs can be obtained from using the following formula (3):

$$pH = 12.8 \cdot \frac{I_{555}^{norm} I_{max}}{I_{456}^{norm} I_{max}} - 5.5, \quad (3)$$

where $I_{555}^{norm} I_{max}$ and $I_{456}^{norm} I_{max}$ are PL intensities with excitation at $\lambda_{ex} = 470$ nm and $\lambda_{ex} = 371$ nm, respectively, both values were normalized on the maximum values of the PL measured for the calibration solutions at boundary pH values (pH 10 and pH 2 for $I_{555}^{norm} I_{max}$ and $I_{456}^{norm} I_{max}$, respectively).

The fitting (3) is ND-specific, i.e. it cannot be extended to NDs with different functional groups on the surface and, correspondingly, with different PLE profiles. Nevertheless, having carried out simple preliminary measurements to get information on the PL associated with $-COOH$ and $-OH$ groups, one can apply similar two-wavelength approach for all-optical pH measurement.

The obtained results are in a good agreement with data presented in [75, 76], where $-COOH$ and $-OH$ groups were specifically created on the surface of DNDs and milled HPHT NDs and their PL was shown to be pH sensitive in the range 2–5 due to $-COOH$ and in the range from 9 to 12.5 due to $-OH$ groups. However, at neutral pH values PL was pH-insensitive, whereas in our case the pH dependence of PL is observed in the entire range (from 2.14 to 10.56). This is because the surface of LHDP-produced NDs used in this study is decorated with C=O containing ketones, carboxylic anhydrides, and carboxyl groups bonded to sp^2 -domains of

various sizes and different combinations of defects, which possibly expands the range of pH sensitivity far beyond the operating range of pure $-COOH$ and $-OH$ groups, mentioned in [76] as pK_a of carboxylic groups strongly depends on the molecule it is bonded to [77].

4. Conclusions

A systematic study of the NDs produced by pulsed laser ablation allows us to demonstrate that there are independent PL centers in the ND shell that can be used for all-optical pH sensing. The performed spectroscopic characterization of NDs reveals that NDs comprise sp^3 cubic core covered with sp^2 -disordered clusters having size of 0.62 nm and decorated with wide range of oxygen-containing surface groups, including hydroxyl, ketone, carboxylic anhydride and carboxyl groups, without a pronounced predominance of any of them. It imparts the NDs with specific spectroscopic properties and thus determine their possible sensing applications. Presence of oxygen-containing groups determines excitation-wavelength-dependent PL of NDs. Spectra fitting with Gaussian profiles gives several independent surface PL centers, whose position is characterized by a slight red shift with the increase of the excitation wavelength.

For $-OH$ PL-centers, PL intensity is a nonlinear function of the ND concentration reaching saturation at concentrations higher than 0.01%, while the characteristic PL lifetimes $\tau_{1,2}$ are concentration independent. For carboxyl PL-centers, PL intensity linearly depends on the NDs concentration and deviates from a linear profile only at the concentration of 0.04% and higher. Characteristic lifetimes of the $-COOH$ PL centers depend on the NDs concentrations from 0.04% and higher. Spectroscopic properties of these PL centers ($-OH$ and $-COOH$) along with their involvement in hydration process and pH-dependence were successfully applied for an all-optical pH-sensing approach. Using $-OH$ PL intensity decrease and $-COOH$ PL intensity increase with the pH growth, we have derived a formula that allows one to determine the pH of the solution using the ratio of these intensities.

Using decorated graphitic shell of NDs for efficient pH sensing is beneficial also because it leaves color centers in diamonds for more challenging sensing, extremely vital for the biological system, such as defining local changes in the membrane potential, currents through the membrane, energy consumption by protein complexes, local temperature, etc, shifting a simpler problem of pH determination to surface groups.

Along with other outstanding NDs properties such as their inertness with respect to biological objects, PL stability, non-toxicity unlike organic dyes, no special handling and storage requirements, it makes NDs strong competitor to other known pH sensing solutions for *in vitro* and *in vivo* applications.

Acknowledgments

This work was supported by Academy of Finland (Flagship Programme PREIN, decision 320166), Horizon 2020 RISE

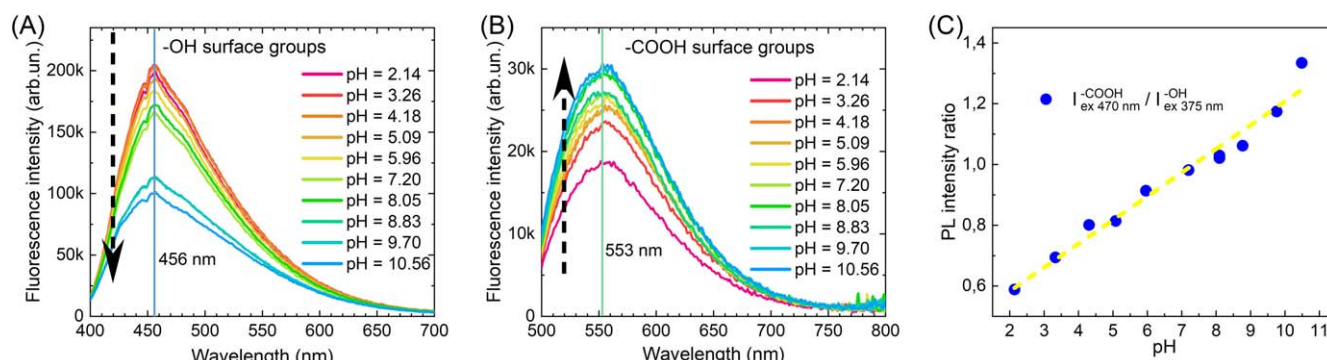


Figure 7. pH screening with 0.01% ND water suspension: (A) 'Blue' PL spectra excited at 375 nm and (B) 'Orange' PL spectra excited at 470 nm, (C) pH calibration curve.

DiSeTCom (Project № 823728) and Horizon Europe FLORIN (Project № 101086142). The authors are grateful to B Zousman and O Levinson (Ray Technology Ltd, Israel) for providing the samples. The authors would like to thank prof. Andrey Chuvilin (CIC nanoGUNE) for TEM microstructure characterization.

Data availability statement

All data that support the findings of this study are included within the article (and any supplementary files).

Supporting information

The Supporting Information is available free of charge and contains the following sections: TEM of NDs; AFM characterization of NDs; ATR-FTIR; Supposed model of NDs and their structure characterization; PLE-mapping of TDW; PL spectra fitting; The dependence of PL characteristics on the pH values.

Author contributions

LG, TK, RK and PK worked out the concept of the research. LG, YP, and AB conceived and designed the experimental study. AFM measurements and data analysis was performed by MJ. LG performed Raman and SERS measurements. IM performed ATR-FTIR spectroscopic analysis. Fluorescence steady-state and time-resolved spectroscopic analysis was conducted with equal contribution of YP, LG, TK, and RK. PLE measurements and data analysis were performed by DS, YP and LG. pH study design and implementation of the experiment were carried out by AB, YP and LG. The manuscript was written by YP, LG and RK. TK, YS and PK provided manuscript review and editing. All authors have approved the final version of the manuscript.

ORCID iDs

Yaraslau Padrez <https://orcid.org/0000-0003-0852-6579>
Lena Golubewa <https://orcid.org/0000-0003-2125-6366>

Anastasiya Bahdanava <https://orcid.org/0000-0002-2586-8151>

Marija Jankunec <https://orcid.org/0000-0002-1119-4467>

Ieva Matulaitiene <https://orcid.org/0000-0001-7664-2331>

Renata Karpicz <https://orcid.org/0000-0001-5884-4538>

Tatsiana Kulahava <https://orcid.org/0000-0002-1113-7323>

Yuri Svirko <https://orcid.org/0000-0002-2927-6233>

Polina Kuzhir <https://orcid.org/0000-0003-3689-0837>

References

- [1] Jelezko F and Wrachtrup J 2006 Single defect centres in diamond: a review *Phys. Status Solidi (a)* **203** 3207–25
- [2] Barnard A S 2014 Distribution, Diffusion and Concentration of Defects in Colloidal Diamond *Nanoscience & Nanotechnology Series* ed O A Williams (Cambridge: Royal Society of Chemistry) ch 1 pp 1–26
- [3] Panich A M, Sergeev N A and Goren S D 2020 Location of paramagnetic defects in detonation nanodiamond from proton spin-lattice relaxation data *Solid State Nucl. Magn. Reson.* **105** 101624
- [4] Malykhin S, Mindarava Y, Ismagilov R, Jelezko F and Obraztsov A 2022 Control of NV, SiV and GeV centers formation in single crystal diamond needles *Diam. Relat. Mater.* **125** 109007
- [5] Yu O V, Zargaleh A, Treussart S, Takai F, Romanov K, Shakhov F M N M and Baldycheva A 2019 Nitrogen impurities and fluorescent nitrogen-vacancy centers in detonation nanodiamonds: identification and distinct features *J. Opt. Technol.* **86** 1
- [6] Tisler J et al 2009 Fluorescence and spin properties of defects in single digit nanodiamonds *ACS Nano* **3** 1959–65
- [7] Campbell B, Choudhury W, Mainwood A, Newton M and Davies G 2002 Lattice damage caused by the irradiation of diamond *Nucl. Instrum. Methods Phys. Res. A* **476** 680–5
- [8] Yavkin B V, Zverev D G, Mamin G V, Gafurov M R and Orlinskii S B 2019 Influence of the chemical modification of the nanodiamond surface on electron paramagnetic resonance/electron-nuclear double resonance spectra of intrinsic nitrogen defects *J. Phys. Chem. C* **123** 22384–9
- [9] Golubewa L et al All-optical thermometry with NV and SiV color centers in biocompatible diamond microneedles *Adv. Opt. Mater.* **n/a** 2200631
- [10] Fan J-W et al 2018 Germanium-vacancy color center in diamond as a temperature sensor *ACS Photon.* **5** 765–70

- [11] Neumann P *et al* 2013 High-precision nanoscale temperature sensing using single defects in diamond *Nano Lett.* **13** 2738–42
- [12] Bolshedvorskii S V *et al* 2019 Single silicon vacancy centers in 10 nm diamonds for quantum information applications *ACS Appl. Nano Mater.* **2** 4765–72
- [13] Yu S-J, Kang M-W, Chang H-C, Chen K-M and Yu Y-C 2005 Bright fluorescent nanodiamonds: no photobleaching and low cytotoxicity *J. Am. Chem. Soc.* **127** 17604–5
- [14] Perona Martínez F, Nusantara A C, Chipaux M, Padamati S K and Schirhagl R 2020 Nanodiamond relaxometry-based detection of free-radical species when produced in chemical reactions in biologically relevant conditions *ACS Sens.* **5** 3862–9
- [15] Wu K *et al* 2022 Applying NV center-based quantum sensing to study intracellular free radical response upon viral infections *Redox Biol.* **52** 102279
- [16] Nie L *et al* 2022 Quantum sensing of free radicals in primary human dendritic cells *Nano Lett.* **22** 1818–25
- [17] Mzyk A, Ong Y, Ortiz Moreno A R, Padamati S K, Zhang Y, Reyes-San-Martin C A and Schirhagl R 2022 Diamond color centers in diamonds for chemical and biochemical analysis and visualization *Anal. Chem.* **94** 225–49
- [18] Głowacki M J, Sawczak M, Wcisło A, Ficek M and Bogdanowicz R 2020 pH-dependency of the physical properties of the nitrogen-vacancy centers in diamonds *Biophotonics Congress: Biomedical Optics 2020 (Translational, Microscopy, OCT, OTS, BRAIN)* (Washington, DC: OSA Technical Digest (Optica Publishing Group, 2020)) 978-1-943580-74-3 (<https://doi.org/10.1364/TRANSLATIONAL.2020.JTh2A.11>)
- [19] Shang L, Nienhaus K and Nienhaus G U 2014 Engineered nanoparticles interacting with cells: size matters *J. Nanobiotechnol.* **12** 5
- [20] Li W, Kaminski Schierle G S, Lei B, Liu Y and Kaminski C F 2022 Fluorescent nanoparticles for super-resolution imaging *Chem. Rev.* **122** 12495–543
- [21] Hao J, Pan L, Gao S, Fan H and Gao B 2019 Production of fluorescent nano-diamonds through femtosecond pulsed laser ablation *Opt. Mater. Express* **9** 4734
- [22] Qin J-X, Yang X-G, Lv C-F, Li Y-Z, Liu K-K, Zang J-H, Yang X, Dong L and Shan C-X 2021 Nanodiamonds: synthesis, properties, and applications in nanomedicine *Mater. Des.* **210** 110091
- [23] Shenderova O and Nunn N 2017 *Production and Purification of Nanodiamonds Nanodiamonds* (Amsterdam: Elsevier) 2 pp 25–56
- [24] Dolmatov V Y 2018 The influence of detonation synthesis conditions on the yield of condensed carbon and detonation nanodiamond through the example of using TNT-RDX explosive mixture *J. Superhard Mater.* **40** 290–4
- [25] Mitev D P, Townsend A T, Paull B and Nesterenko P N 2014 Screening of elemental impurities in commercial detonation nanodiamond using sector field inductively coupled plasma-mass spectrometry *J. Mater. Sci.* **49** 3573–91
- [26] Aleksenskiy A E, Eydelman E D and Vul' A Y 2011 Deagglomeration of detonation nanodiamonds *Nanosci. Nanotechnol. Lett.* **3** 68–74
- [27] Terada D, So F T K, Hattendorf B, Yanagi T, Ōsawa E, Mizuochi N, Shirakawa M, Igarashi R and Segawa T F 2022 A simple and soft chemical deaggregation method producing single-digit detonation nanodiamonds *Nanoscale Adv.* **4** 2268–77
- [28] Zousman B and Levinson O 2012 Monodispersed nanodiamonds produced by laser ablation *MRS Proc.* **1452** mrss12-1452-ff07-06
- [29] Zousman B and Levinson O 2014 Pure Nanodiamonds Produced by Laser-Assisted Technique *RSC Nanoscience and Nanotechnology* **2014** 112–27
- [30] Igarashi K, Shoji Y, Sekine-Suzuki E, Ueno M, Matsumoto K, Nakanishi I and Fukui K 2022 Importance of locations of iron ions to elicit cytotoxicity induced by a fenton-type reaction *Cancers* **14** 3642
- [31] Ge C, Li Y, Yin J-J, Liu Y, Wang L, Zhao Y and Chen C 2012 The contributions of metal impurities and tube structure to the toxicity of carbon nanotube materials *NPG Asia Mater.* **4** e32–32
- [32] Basso L, Cazzanelli M, Orlandi M and Miotello A 2020 Nanodiamonds: synthesis and application in sensing, catalysis, and the possible connection with some processes occurring in space *Appl. Sci.* **10** 4094
- [33] Tian Y, Nusantara A C, Hamoh T, Mzyk A, Tian X, Perona Martinez F, Li R, Permentier H P and Schirhagl R 2022 Functionalized fluorescent nanodiamonds for simultaneous drug delivery and quantum sensing in HeLa cells *ACS Appl. Mater. Interfaces* **14** 39265–73
- [34] Fujisaku T, Tanabe R, Onoda S, Kubota R, Segawa T F, So F T-K, Ohshima T, Hamachi I, Shirakawa M and Igarashi R 2019 pH nanosensor using electronic spins in diamond *ACS Nano* **13** 11726–32
- [35] Williams O A 2014 *Nanodiamond* (Cambridge, UK: Royal Society of Chemistry) (*Nanoscience & Nanotechnology*) (<https://doi.org/10.1039/9781849737616>)
- [36] Golubewa L *et al* 2020 Surface-enhanced raman spectroscopy of organic molecules and living cells with gold-plated black silicon *ACS Appl. Mater. Interfaces* **12** 50971–84
- [37] Golubewa L *et al* 2022 Visualizing hypochlorous acid production by human neutrophils with fluorescent graphene quantum dots *Nanotechnology* **33** 095101
- [38] Petit T and Puskar L 2018 FTIR spectroscopy of nanodiamonds: Methods and interpretation *Diam. Relat. Mater.* **89** 52–66
- [39] Țucureanu V, Matei A and Avram A M 2016 FTIR Spectroscopy for Carbon Family Study *Crit. Rev. Anal. Chem.* **46** 502–20
- [40] Barth A 2007 Infrared spectroscopy of proteins *Biochim. Biophys. Acta (BBA)—Bioenergetics* **1767** 1073–101
- [41] Gaidukevič J, Pauliukaitė R, Niaura G, Matulaitienė I, Opuchovič O, Radzevič A, Astromskas G, Bukauskas V and Barkauskas J 2018 Synthesis of reduced graphene oxide with adjustable microstructure using regioselective reduction in the melt of boric acid: relationship between structural properties and electrochemical performance *Nanomaterials* **8** 889
- [42] Zou Q, Li Y G, Zou L H and Wang M Z 2009 Characterization of structures and surface states of the nanodiamond synthesized by detonation *Mater. Charact.* **60** 1257–62
- [43] Goldstein M 1981 Infrared characteristic group frequencies *Endeavour* **5** 90–1
- [44] Ravindra S, Mohan Y M, Varaprasad K, Reddy N N, Vimala K and Raju K M 2009 Surfactant-Modified Poly (acrylamide- *co* -acrylamido propane sulphonic acid) Hydrogels *Int. J. Polym. Mater.* **58** 278–96
- [45] Hasan I, Khan R A, Alharbi W, Alharbi K H and Alsalmeh A 2019 *In Situ* copolymerized polyacrylamide cellulose supported Fe₃O₄ magnetic nanocomposites for adsorptive removal of Pb(II): artificial neural network modeling and experimental studies *Nanomaterials* **9** 1687
- [46] Mayo D W, Miller F A and Hannah R W 2004 *Course Notes on the Interpretation of Infrared and Raman Spectra* (New York: Wiley)
- [47] Tyurmina A V, Apolonskaya I A, Kulakova I I, Kopylov P G and Obratsov A N 2010 Thermal purification of detonation diamond *J. Synch. Investig.* **4** 458–63
- [48] Thapliyal V, Alabdulkarim M E, Whelan D R, Mainali B and Maxwell J L 2022 A concise review of the Raman spectra of carbon allotropes *Diam. Relat. Mater.* **127** 109180

- [49] Zaitsev A M 2013 *Optical Properties of Diamond* (Berlin, Heidelberg: Springer) 1 (<https://doi.org/10.1007/978-3-662-04548-0>)
- [50] Perevedentseva E, Karmenyan A, Chung P-H and Cheng C-L 2005 Surface-enhanced Raman spectroscopy of nanodiamond particles on silver *J. Vac. Sci. Technol. B* **23** 1980
- [51] Aleksenskii A E, Osipov V Y, Vul' A Y, Ber B Y, Smirnov A B, Melekhin V G, Adriaenssens G J and Iakoubovskii K 2001 Optical properties of nanodiamond layers *Phys. Solid State* **43** 145–50
- [52] Osswald S, Mochalin V N, Havel M, Yushin G and Gogotsi Y 2009 Phonon confinement effects in the Raman spectrum of nanodiamond *Phys. Rev. B* **80** 075419
- [53] Mochalin V N, Shenderova O, Ho D and Gogotsi Y 2012 The properties and applications of nanodiamonds *Nat. Nanotech.* **7** 11–23
- [54] Aprà P, Mino L, Battiato A, Olivero P, Sturari S, Valsania M C, Varzi V and Picollo F 2021 Interaction of nanodiamonds with water: impact of surface chemistry on hydrophilicity, aggregation and electrical properties *Nanomaterials* **11** 2740
- [55] Barnard A S, Russo S P and Snook I K 2003 Structural relaxation and relative stability of nanodiamond morphologies *Diam. Relat. Mater.* **12** 1867–72
- [56] Wu J, Wang P, Wang F and Fang Y 2018 Investigation of the microstructures of graphene quantum dots (GQDs) by surface-enhanced Raman spectroscopy *Nanomaterials* **8** 864
- [57] Ferrari A C and Robertson J 2000 Interpretation of Raman spectra of disordered and amorphous carbon *Phys. Rev. B* **61** 14095–107
- [58] Li Z Z, Zhang Y, Ma L, Tang G D, Wu G H and Hu F X 2022 A new explanation on valence electron structure of C, Si, and Ge crystals with diamond structure based on photoelectron spectra *J. Electron. Spectrosc. Relat. Phenom.* **254** 147153
- [59] Lifshitz Y 1999 Diamond-like carbon—present status *Diam. Relat. Mater.* **8** 1659–76
- [60] Aleksenskii A E, Vul' A Y, Konyakhin S V, Reich K V, Sharonova L V and Eidel'man E D 2012 Optical properties of detonation nanodiamond hydrosols *Phys. Solid State* **54** 578–85
- [61] Yeh T-F, Huang W-L, Chung C-J, Chiang I-T, Chen L-C, Chang H-Y, Su W-C, Cheng C, Chen S-J and Teng H 2016 Elucidating quantum confinement in graphene oxide dots based on excitation-wavelength-independent photoluminescence *J. Phys. Chem. Lett.* **7** 2087–92
- [62] Sorensen C M 2022 Rayleigh scattering *Light Scattering and Absorption by Particles: The Q-space approach*
- [63] Mishchenko M I, Travis L D and Lacis A A 2002 *Absorption, and Emission of Light by Small Particles | Atmospheric science and meteorology* (Cambridge, UK: Cambridge University Press) Anon Scattering
- [64] Bohren C F and Huffman D R 1998 *Absorption and Scattering of Light by Small Particles* (New York: Wiley)
- [65] Eidelman E D, Siklitsky V I, Sharonova L V, Yagovkina M A, Vul' A Y, Takahashi M, Inakuma M, Ozawa M and Ōsawa E 2005 A stable suspension of single ultrananocrystalline diamond particles *Diam. Relat. Mater.* **14** 1765–9
- [66] Hottechamps J, Noblet T, Brans A, Humbert C and Dreesen L 2020 How quantum dots aggregation enhances Förster resonant energy transfer *Chem. Phys. Chem.* **21** 853–62
- [67] Noblet T, Dreesen L, Hottechamps J and Humbert C 2017 A global method for handling fluorescence spectra at high concentration derived from the competition between emission and absorption of colloidal CdTe quantum dots *Phys. Chem. Chem. Phys.* **19** 26559–65
- [68] Jameson D M 2014 *Introduction to Fluorescence* (Boca Raton, FL: CRC Press)
- [69] Kozawa D, Zhu X, Miyauchi Y, Mouri S, Ichida M, Su H and Matsuda K 2014 Excitonic photoluminescence from nanodisc states in graphene oxides *J. Phys. Chem. Lett.* **5** 1754–9
- [70] Lee K-M et al 2013 Excitation-dependent visible fluorescence in decameric nanoparticles with monoacylglycerol cluster chromophores *Nat. Commun.* **4** 1544
- [71] Xiao J, Liu P, Li L and Yang G 2015 Fluorescence origin of nanodiamonds *J. Phys. Chem. C* **119** 2239–48
- [72] Wu W, Cao J, Zhong M, Wu H, Zhang F, Zhang J and Guo S 2019 Separating graphene quantum dots by lateral size through gel column chromatography *RSC Adv.* **9** 18898–901
- [73] Turcheniuk K and Mochalin V N 2017 Biomedical applications of nanodiamond (review) *Nanotechnology* **28** 252001
- [74] Jang M-H, Song S H, Ha H D, Seo T S, Jeon S and Cho Y-H 2017 Origin of extraordinary luminescence shift in graphene quantum dots with varying excitation energy: an experimental evidence of localized sp² carbon subdomain *Carbon* **118** 524–30
- [75] Reineck P, Lau D W M, Wilson E R, Nunn N, Shenderova O A and Gibson B C 2018 Visible to near-IR fluorescence from single-digit detonation nanodiamonds: excitation wavelength and pH dependence *Sci. Rep.* **8** 2478
- [76] Vervald A M, Lachko A V, Kudryavtsev O S, Shenderova O A, Kuznetsov S V, Vlasov I I and Dolenko T A 2021 Surface photoluminescence of oxidized nanodiamonds: influence of environment pH *J. Phys. Chem. C* **125** 18247–58
- [77] Pozdnyakov I P, Pigliucci A, Tkachenko N, Plyusnin V F, Vauthey E and Lemmetyinen H 2009 The photophysics of salicylic acid derivatives in aqueous solution *J. Phys. Org. Chem.* **22** 449–54